15th IFK
Proc. of the 15th International Fluid Power Conference <Symposium/Conference>
<DOI>

Feasibility of Electro-Hydrostatic Actuators in Wheel Loader Application: A Case Study Focusing on Energy Efficiency, Controllability and Thermal Behaviour

Vili Vironmäki*, Ville Raunio, Mikko Huova and Petteri Multanen

Innovative Hydraulics and Automation, Tampere University, Tampere, Finland
* Corresponding author: vili.vironmaki@tuni.fi

Abstract.

Hydraulic actuators are extensively applied in non-road mobile machinery (NRMM) owing to their high power-to-weight ratio, robustness, and compact design. Conventional systems, however, exhibit throttling losses in control valves, which limit efficiency. While drivetrain electrification has been widely studied, the electrification of working hydraulics with electro-hydrostatic actuators (EHAs) remains less explored. EHAs eliminate throttling losses and enable energy regeneration, yet their suitability for wheel loaders has not been thoroughly assessed. This study investigates the feasibility of EHAs in wheel loaders through MATLAB/Simulink simulations using measured load cycle data of a typical short Y-cycle. EHA-based and conventional systems are compared with respect to energy efficiency, while thermal behaviour under simulated power losses is analysed using a lumped-parameter model. The results indicate that EHAs exhibit satisfactory position tracking accuracy and markedly improve energy efficiency, while thermal management remains an aspect that must be considered for reliable operation. Thus, EHAs show considerable promise for NRMM applications, provided that they are implemented properly, including adequate cooling.

Keywords. Electro-hydrostatic actuator, electrification, wheel loader, energy efficiency, thermal management.

1. INTRODUCTION

Hydraulic actuators are widely used in non-road mobile machinery (NRMM), such as wheel loaders and excavators, due to their high power density, robustness, and compact design [1, 2]. However, conventional valve-controlled hydraulics suffer from low overall efficiency because of throttling losses in directional control valves [3]. Meanwhile, stricter emission regulations and the growing demand for energy efficiency highlight the need for alternative hydraulic architectures.

Electrification offers a promising way to meet these requirements. While electric and hybrid drivetrains are already commercially available in NRMM, the electrification of working hydraulics remains less developed [4]. Electro-hydrostatic actuators (EHAs), in which an electric motor drives a hydraulic pump that directly supplies the actuator without control valves, can eliminate throttling losses and enable energy recovery [5, 6]. EHAs have been investigated in several NRMM applications, including mining loaders and excavators, focusing on efficiency improvements and alternative EHA concepts, such as high-speed implementations [7–11]. In wheel loader studies, EHAs have demonstrated significant efficiency gains over load-sensing (LS) systems but also indicated a need for thermal analysis [12].

Thermal behaviour is critical for closed-circuit EHAs, as they lack a reservoir that plays an important role in heat dissipation in conventional hydraulic systems. Elevated oil temperature reduces viscosity, accelerates component wear, and shortens the lifespan of hydraulic oil, thereby making temperature prediction essential during system design. High-fidelity thermal models exist but are computationally demanding for long duty cycles and often unnecessary in early-stage studies [13]. Lumped-parameter models provide a practical compromise, reducing data requirements and computational effort while maintaining sufficient accuracy [14]. Although thermal simulation studies of EHAs have been reported in the literature, for example by Michel et al. [15, 16], these focus on actuator sizes and load cycles that differ substantially from those encountered in wheel loader applications. Consequently, their results cannot be directly extrapolated to the present case, motivating a dedicated thermal simulation tailored to wheel loader operating conditions.

Most prior work addresses efficiency, controllability, or thermal behaviour in isolation and often relies on single-actuator setups, while also overlooking real load cycle data. However, trade-offs may arise between controllability, losses, and temperature rise, while position tracking accuracy may degrade in multi-actuator systems. This paper evaluates EHAs for wheel loader work functions holistically. Using measured duty-cycle and load data [17], a MATLAB/Simulink model with a high-fidelity mechanical boom representation compares an EHA system with an LS baseline. The analysis focuses on energy efficiency, controllability, and thermal behaviour under realistic load cycles to assess the feasibility of EHA integration in wheel loader application.

The remainder of this paper is organized as follows. Section 2 presents the system overview, including the boom structure and EHAs. Section 3 describes the system modelling. Simulation results are given in Section 4, followed by thermal modelling and analysis in Section 5. Section 6 concludes the paper.

2. OVERVIEW OF THE SYSTEM

The system is a 6-tonne wheel loader performing the short Y-cycle of gravel loading. The boom (Fig. 2.1) includes two primary working actuators: lift cylinders and tilt cylinders, and a pair of stabilising (self-levelling) cylinders that are kinematically linked to the lift mechanism. When the lift cylinders extend, the stabilising cylinders move accordingly and drive the tilt cylinders to maintain bucket orientation. In the proposed architecture, the working actuators are implemented as EHAs.

Each EHA employs single-rod (asymmetric) hydraulic cylinders. The unequal chamber volumes are compensated by differential-flow compensation implemented with check valves, which allow flow from a low-pressure accumulator to meet the additional demand on the rod side. Each actuator is isolated by a normally closed 2/2 poppet valve functioning as an on/off load-holding valve (LHV), included for both safety and efficiency. Relief valves protect the system against overload conditions.

The cylinders are supplied by bidirectional pump/motor units capable of four-quadrant operation. The pumps are driven by permanent magnet synchronous motors (PMSMs), enabling high efficiency and precise control. During motion commands, the load-holding valves are energised (open), and otherwise they hold the load.

In the present work, conventional electric motors and hydraulic pumps with a maximum speed of 4000 rpm are employed. However, decentralized EHA architectures generally require more installation space than centralised hydraulic systems, which must be considered during system design. This limitation may be mitigated by using high-speed drives, as demonstrated in [10], which enable higher power density.

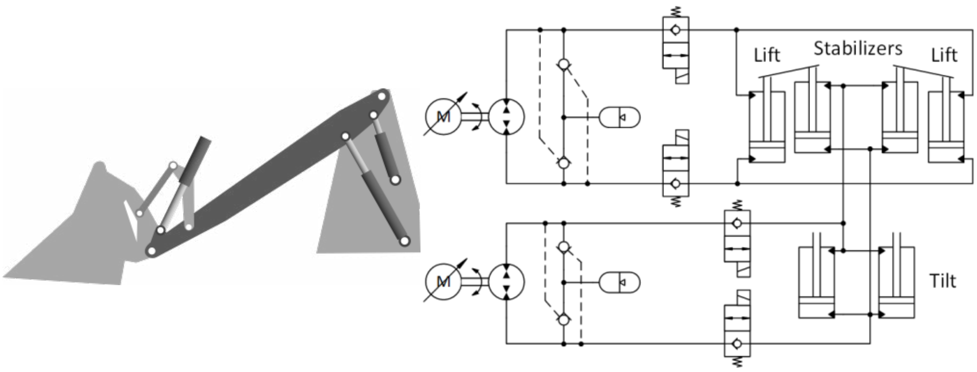

(a) (b)

Figure 2.1. (a) Wheel loader boom with the lift, tilt, and stabilising cylinders highlighted. (b) Simplified hydraulic schematic of the proposed EHA architecture.

3. System Models

This section presents the system modelling. Section 3.1 develops the EHA model. Section 3.2 derives the electric power of the baseline LS system from measured data. Section 3.3 presents the EHA control architecture with PMSM current and speed control in the inner loops and position control in the outer loop.

3.1. EHA Model

The electro-hydrostatic actuators are modelled in MATLAB/Simulink, while the multibody dynamics of the wheel loader boom are represented in Simscape Multibody. The model incorporates boom and bucket inertias, gravitational effects, and linkage geometry. External loads such as payloads are not explicitly modelled but applied as an external force term derived from measured data. Actuator displacements are kinematically coupled to the linkage, and end-stop impacts are neglected as duty cycles remain within the stroke range.

The EHAs consist of a PMSM, an axial piston pump, hydraulic cylinders, accumulators, and auxiliary valves. The PMSM is described in the rotating d–q reference frame as

$$u_d = R_s i_d + L_d \frac{di_d}{dt} - P\omega L_q i_q \qquad u_q = R_s i_q + L_q \frac{di_q}{dt} + P\omega\left(L_d i_d + \phi_f\right) \tag{3.1}$$

$$T_e = \frac{3}{2} P\left(\phi_f i_q + \left(L_d - L_q\right) i_d i_q\right) \tag{3.2}$$

where u_d, u_q are stator voltages, i_d, i_q currents, R_s stator resistance, L_d, L_q inductances, P pole pairs, ω rotor speed, ϕ_f flux linkage (constant), and T_e electromagnetic torque. Motor parameters are taken from the Bosch Rexroth MS2N10-F0BHA (22.4 kW) datasheet [18].

The axial piston pump/motor is first expressed ideally as

$$Q_t = D_p \omega_p \qquad T_t = D_p \Delta p \tag{3.3}$$

where ω_p [rad/s] is the shaft speed, D_p [m^3/rad] the displacement, and $\Delta p = p_A - p_B$ the differential pressure over the pump/motor. Volumetric and mechanical losses are modelled using the analytical formulation of Huova et al. [19]. The actual flow rates to the A and B sides, and the shaft torque, are given by

$$\begin{aligned} Q_A &= Q_t - Q_{il} - Q_{el,A} \\ Q_B &= -Q_t + Q_{il} - Q_{el,B} \end{aligned} \qquad T_p = T_t + T_l \tag{3.4}$$

where Q_{il} and Q_{el} denote the internal and external leakages, and T_l the torque loss. The internal leakage Q_{il} is defined positive from the A-side to the B-side and may reverse direction depending on the pressure difference. External leakages depend on the pressure differences between the line and the accumulator.

Hydraulic cylinder chamber pressures are governed by

$$\frac{dp}{dt} = \frac{B_{eff}}{V}\left(\Sigma Q - \frac{dV}{dt}\right) \tag{3.5}$$

where B_{eff} is the effective bulk modulus, V the chamber volume, and Q the chamber flows. The actuator force is

$$F = A_a p_a - A_b p_b - F_\mu - F_{ext} \tag{3.6}$$

where A_a, A_b are piston areas, p_a, p_b chamber pressures, F_μ friction, and F_{ext} the measured external load. Friction is represented using a Coulomb–viscous–Stribeck model.

The accumulator pressure follows a polytropic gas relation,

$$p_{acc} = \left(\frac{V_0}{V_0 - \int Q_{acc} dt}\right)^n p_0 \qquad Q_{acc} = Q_{el,A} + Q_{el,B} + Q_{RV} - Q_{CV} \tag{3.7}$$

where V_0 is the nominal volume, p_0 the pre-charge pressure, and $n = 1.4$. The accumulators are pre-charged to 4.5 bar, with 6 L for the lift and 10 L for the tilt actuator.

Flow through the three types of orifices is modelled using the same orifice law in (3.8), with component-specific definitions for the opening area A:

- Pilot-operated check valve (POCV): the opening area A depends on the control pressure p_c as defined in (3.9)–(3.10).
- Load-holding valve: the area A is set by the on/off signal u_{LH} according to (3.11).
- Cylinder orifices: the area A is constant.

$$Q = AC_{q,max} \tanh\left(\frac{2\lambda}{\lambda_{crit}}\right) \sqrt{\frac{2|\Delta p|}{\rho}} \operatorname{sign}(\Delta p) \qquad \lambda = \frac{D_h}{\nu} \sqrt{\frac{2|\Delta p|}{\rho}} \tag{3.8}$$

where ρ is the fluid density, $\Delta p = p_1 - p_2$ the pressure difference across the orifice, and $\lambda_{crit} = 1000$ [20]. The flow number λ characterises the laminar–turbulent transition and modifies the discharge coefficient via the hyperbolic tangent term.

For the POCV, the control pressure and area–pressure relationships are defined as

$$p_c = (p_x - p_1)k_p + (p_1 - p_2) \tag{3.9}$$

$$A(p_c) = \begin{cases} A_{leak}, & p_c \leq p_{cr} \\ A_{leak} + k(p_c - p_{cr}), & p_{cr} < p_c < p_{max} \\ A_{max}, & p_c \geq p_{max} \end{cases} \qquad k = \frac{A_{max} - A_{leak}}{p_{max} - p_{cr}} \tag{3.10}$$

The opening area A of both the POCV and LHV follows a first-order lag with a time constant of 0.1 s. The LHV is normally closed and energised according to

$$u_{LH} = \begin{cases} 1, & |\dot{x}_{ref}| > 0 \text{ m/s or } |e_c| > 1 \text{ mm} \\ 0, & \text{otherwise} \end{cases} \tag{3.11}$$

where $\dot{x}_{ref}$ is the commanded actuator velocity and e_c the position error. Simulation parameters are listed in Table 1.

Table 1: Parameters of lift and tilt EHAs

Parameter	Lift	Tilt	Parameter	Lift	Tilt
D_p [cc/rev]	50.7	45	J_{PM} [kg·m^2]	0.0035	0.0025
A_a [cm^2]	100.5	127.2	A_b [cm^2]	68.7	88.0
$C_{q,max}$ [–]	0.7	0.7	s [mm]	640	400
p_{cr} [bar]	0.5	0.5	k_p [–]	3	3
V_0 [L]	6	10	p_0 [bar]	4.5	4.5
f_{sw} [Hz]	2000	2000	ϵ [–]	0.5	0.5

3.2. LS Model

The LS system is used as a reference for comparison with the EHA-based system. Measurement data were obtained from an LS configuration originally driven by a combustion engine [17], but for consistency, the LS system is assumed to be driven by an electric motor operating at constant speed.

Measured pump flow Q_p and pressure p_p are converted into mechanical shaft power using the pump model defined in (3.3)–(3.4). The mechanical shaft power and the corresponding electrical input power are expressed as

$$P_{shaft} = T_p \omega_p \qquad P_{el} = \frac{P_{shaft}}{\eta_{em}(T_p, \omega_p)} \tag{3.12}$$

where $\eta_{em}(T_p, \omega_p)$ is obtained from the manufacturer's efficiency map [21].

3.3. Controller Design

The PMSM in the EHA is controlled by a cascade structure with dq-axis current loops and outer speed loop, all implemented with PI controllers tuned using the method in [22]. The dq-axis currents are regulated by PI controllers with decoupling terms, according to

$$u_q = K_{pc}(i_{q,ref} - i_q) + K_{ic} \int (i_{q,ref} - i_q) dt + \omega_e (L_d i_d + \phi_f) \tag{3.13}$$

$$u_d = K_{pc}(i_{d,ref} - i_d) + K_{ic} \int (i_{d,ref} - i_d) dt - \omega_e L_q i_q \tag{3.14}$$

where $i_{d,ref} = 0$ and $\omega_e = P\omega$. The controller gains are

$$K_{pc} = L_s \omega_c \qquad K_{ic} = R_s \omega_c \tag{3.15}$$

with the current control bandwidth ω_c set one decade below the inverter switching frequency f_{sw}.

The electromagnetic torque is generated by the q-axis current i_q, which serves as the control variable in the outer speed loop. The PI speed controller generates the current reference as

$$i_{q,ref} = K_{ps}(\omega_{ref} - \omega) + K_{is} \int (\omega_{ref} - \omega) dt \tag{3.16}$$

$$K_{ps} = \frac{J_{tot} \omega_s}{K_t} \qquad K_{is} = K_{ps} \frac{\omega_s}{5} \tag{3.17}$$

where J_{tot} is the total inertia, K_t the torque constant, and $\omega_s = \omega_c/5$.

The motor speed reference combines position feedback, velocity feedforward, and dynamic pressure feedback, conditioned by the LHV logic:

$$\omega_{ref} = \begin{cases} K_\omega (u_{fb} + u_{ff} - u_{pf}), & u_{LH} = 1 \\ 0, & \text{otherwise} \end{cases} \tag{3.18}$$

This ensures that the motor is commanded only when the LHV is energised, preventing line pressurisation when the valves are closed.

The velocity conversion ratio between cylinder and motor is defined as

$$K_\omega = \begin{cases} A_a/D_p, & \Delta p_L > 0 \\ A_b/D_p, & \text{otherwise} \end{cases} \tag{3.19}$$

where D_p is in [m^3/rad]. The position feedback is implemented using proportional control, while the velocity feedforward term directly applies the commanded velocity as

$$u_{fb} = K_p\left(x_{ref} - x\right) \qquad u_{ff} = K_{ff} v_{ref} \tag{3.20}$$

Damping is increased using high-pass filtered load-pressure feedback:

$$u_{pf} = \frac{K_{pf}s}{s + \omega_{pf}} \Delta p_L \qquad \Delta p_L = p_a - \frac{A_b}{A_a} p_b \tag{3.21}$$

This control approach follows [23], with the addition of the LHV logic. The overall controller is illustrated in Fig. 3.1, and the controller parameters are listed in Table 2.

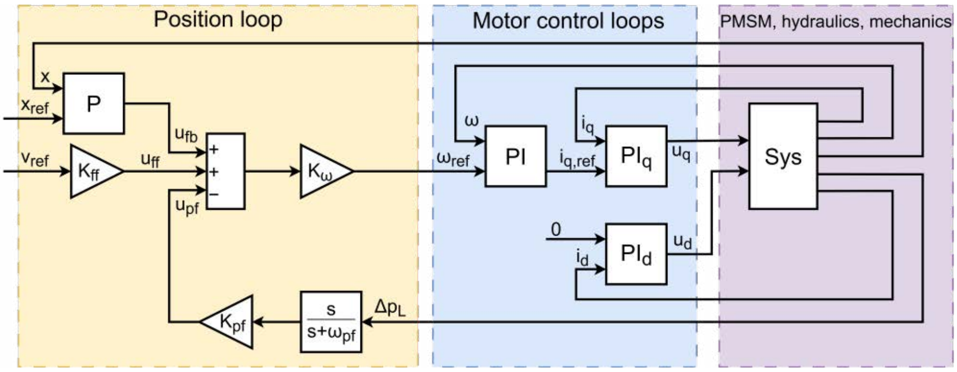

Figure 3.1. Control structure of the EHA showing the position control loop and the motor speed and current control loops. The decoupling terms of the inner PI$_q$ and PI$_d$ current controllers are omitted for clarity.

Table 2: Controller parameters

Parameter	Lift	Tilt	Parameter	Lift	Tilt
K_p [1/s]	2	4	K_{ff} [–]	1	0.5
ω_{pf} [rad/s]	6.60	8.70	K_{pf} [m·s^{-1}·bar^{-1}]	$1.5 \cdot 10^{-4}$	$2 \cdot 10^{-4}$
K_{ps} [A·s/rad]	2.28	2.15	K_{is} [A/rad]	115	108
K_{pc} [V/A]	3.15	3.15	K_{ic} [V·A^{-1}·s^{-1}]	106	106

4. Simulation Results

This section presents simulation results of the proposed EHA architecture for wheel loader application. Position references for the lift and tilt cylinders were derived from Y-cycle measurements on a real machine. The analysis focuses on actuator controllability and energy efficiency, while thermal behaviour is discussed separately in Section 5.

4.1. Controllability

Tracking performance is evaluated using the short Y-cycle reference (Fig. 4.1). The actuators follow the position references with satisfactory accuracy. The maximum tracking errors are below 4 mm for the lift actuator and 29 mm for the tilt actuator, with corresponding root mean square (RMS) errors of 1.3 mm and 5.4 mm, respectively. During the load-holding phase, errors remain below 1 mm due to the control rule defined in equation (3.11). The tilt EHA exhibits higher position errors than the lift actuator because of the lift–tilt coupling through the stabilising cylinder. This coupling introduces disturbances in the position loop, requiring the controller to prioritise feedback compensation over faster velocity feedforward action, for which $K_{ff} = 0.5$ is applied in the tilt actuator. Despite these larger deviations, the achieved accuracy can be considered sufficient for typical load-handling tasks.

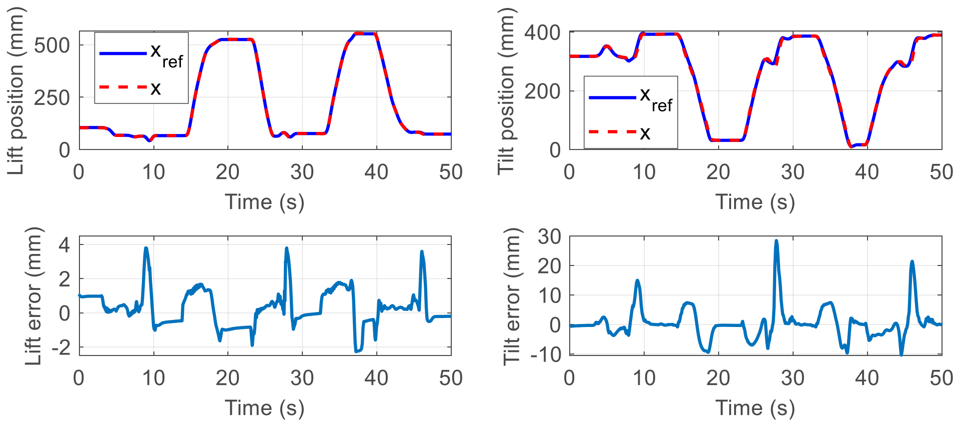

Figure 4.1. Position-tracking performance of lift and tilt actuators during the Y-cycle.

The dynamic behaviour during load-holding valve operation is illustrated in Fig. 4.2. When the LHV is closed, the actuator chamber is isolated from the line, allowing it to hold the load while a pressure difference of approximately 7.6 MPa gradually builds up between the chamber (p_a) and the connected line (p_{la}). When the valve opens, this pressure imbalance induces a brief cylinder motion as the pressures equalise. The resulting position deviation is minor and does not significantly affect overall performance.

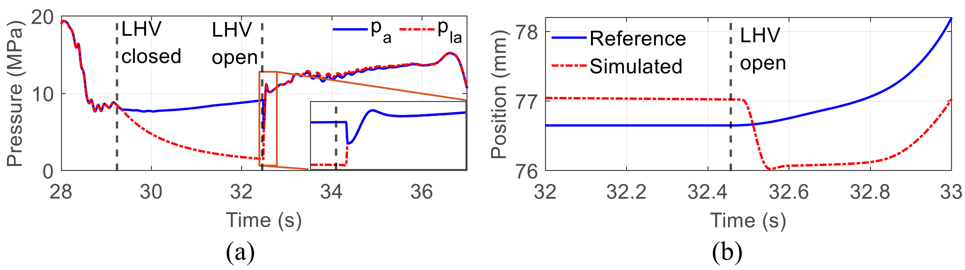

Figure 4.2. (a) Pressure dynamics in the A-chamber and connected line during load-hold valve operation. (b) Position tracking after valve opening.

4.2. Energy Analysis

Energy efficiency over the load cycle is evaluated and compared with the LS baseline. The instantaneous mechanical power of the cylinder and the electrical power of the PMSM are

$$P_{cyl} = F_{cyl}\dot{x} \qquad\qquad P_{el} = T_e\omega + P_{Cu} + P_{Fe} \tag{4.1}$$

where F_{cyl} is the cylinder force and $\dot{x}$ the piston velocity. Copper and iron losses are

$$P_{Cu} = \frac{3}{2}R_S\left(i_d^2 + i_q^2\right) \qquad\qquad P_{Fe} = \frac{K_{Fe}m_{EM}\epsilon}{1000\pi^{3/2}}|P\omega|^{3/2} \tag{4.2}$$

with $K_{Fe} = 4\ \mathrm{W/kg}$ as the core loss per unit mass of sheet metal, m_{EM} the PMSM mass, and ϵ the sheet metal fraction [24]. The iron loss model provides only a simplified approximation. The EHA losses are primarily determined by the component efficiencies, unlike in conventional systems where throttling losses dominate. Therefore, Fig. 4.3 shows the efficiency maps of the main components together with their operation points over the lift actuator load cycle, providing an indication of the achievable overall efficiency. The motor efficiency map in Fig. 4.3a is based on the loss calculations in (4.2), while the pump map in Fig. 4.3b is derived from the model described in (3.3)–(3.4).

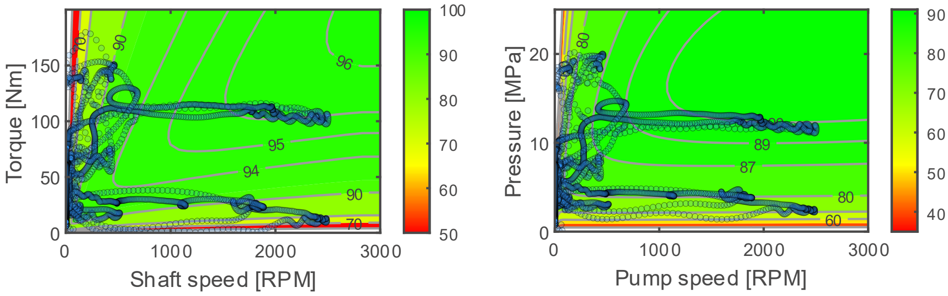

Figure 4.3. (a) Electric motor efficiency map and (b) lift pump efficiency map. Blue circles denote the operation points over the lift actuator load cycle.

Inverter losses are considered under the assumption of a constant inverter efficiency:

$$P_{DC} = \begin{cases} \dfrac{P_{el}}{\eta_{inv}}, & P_{el} \geq 0 \\ \eta_{inv}P_{el}, & P_{el} < 0 \end{cases} \qquad\qquad \eta_{inv} = 0.97 \tag{4.3}$$

The cycle energies and efficiency are defined as

$$E_{in} = \int P_{DC}dt \qquad\qquad E_{out} = \int P_{cyl}dt \qquad\qquad \eta = E_{out}/E_{in} \tag{4.4}$$

Positive P_{cyl} corresponds to load-resistive phases, whereas negative values indicate load-assistive phases. As the boom motion is periodic, the net work on the structure's own mass over a cycle is zero, and only the useful payload work is considered as output.

Figure 4.4 illustrates motor and cylinder powers for lift and tilt EHAs during the short Y-cycle. In load-resistive phases the motor receives electrical input ($P_{el} > 0$) and the cylinder outputs mechanical power ($P_{cyl} > 0$). In load-assistive phases the load drives the actuator ($P_{cyl} < 0$) and the motor operates regeneratively ($P_{el} < 0$). For the tilt actuator, brief resistive segments with $P_{out} > P_{in}$ occur because the lift actuator momentarily drives the tilt cylinders through the stabilising cylinders.

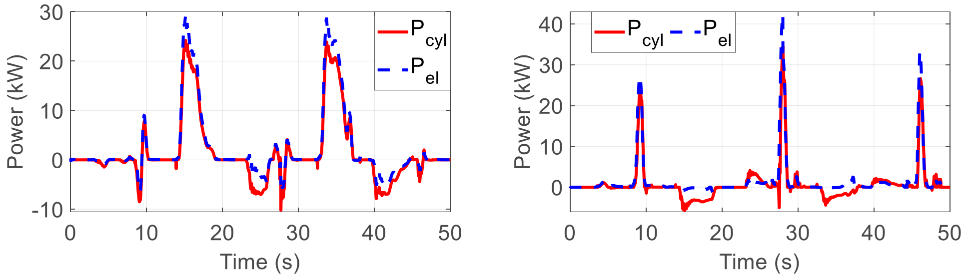

(a) (b)

Figure 4.4. Motor electrical power P_{el} and cylinder mechanical power P_{cyl} for lift (a) and tilt (b) EHAs during the Y-cycle.

Figure 4.5 compares lift–tilt powers for LS and EHA systems, and Fig. 4.6 presents the corresponding cumulative energies. For the Y-cycle, the EHA requires 31.9 % of the electrical input of the LS system, yielding efficiencies of $\eta_{LS} = 0.17$ and $\eta_{EHA} = 0.55$. These results demonstrate that the EHA is substantially more efficient than the LS system.

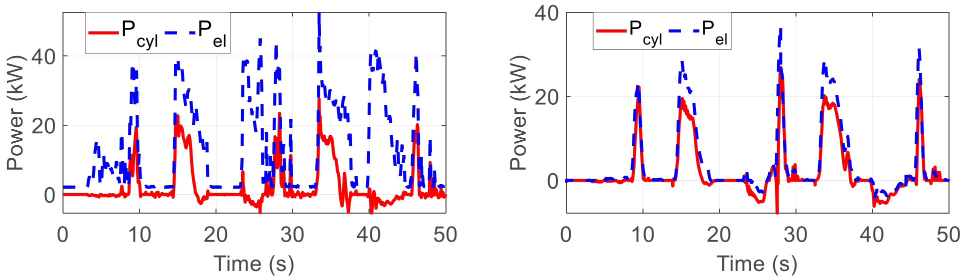

(a) (b)

Figure 4.5. Motor electrical power P_{el} and cylinder mechanical power P_{cyl} for LS (a) and EHA (b). Powers are sums over lift and tilt actuators.

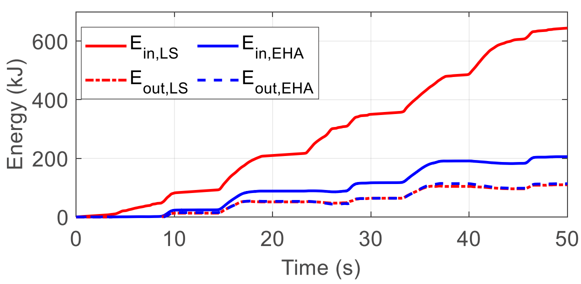

Figure 4.6. Cumulative electrical input energies E_{in} and useful cylinder outputs E_{out} for LS and EHA systems. Energies are sums over lift and tilt actuators.

Component-level losses are obtained by separating resistive and assistive intervals (Fig. 4.7). From the PMSM electrical input of 2.89 kW, 77.0 % is converted into useful mechanical output at the cylinder (2.22 kW). The remainder is dissipated in the motor (6.0%), pump/motor (10.9%), throttling (1.9%), and cylinder friction (5.6%). During assistive phases, the boom's potential energy provides 1.13 kW of mechanical input, of which 47.7 % (538 W) is transferred back to the inverter, while the rest is lost due to electrical, hydraulic, and mechanical losses as well as accumulator charging.

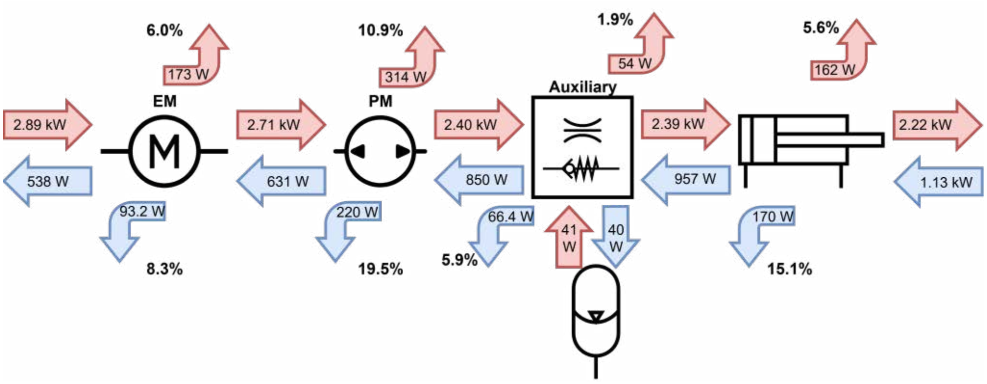

Figure 4.7. Component-level power flows of the lift actuator (EHA). Red = load-resistive (lifting), blue = load-assistive (lowering, regeneration).

Over a full Y-cycle, the mean loss powers are

$$\begin{aligned} P_{cyl,loss} &= 162\ \mathrm{W} + 170\ \mathrm{W} = 332\ \mathrm{W} \\ P_{aux,loss} &= 54\ \mathrm{W} + 66.4\ \mathrm{W} = 120.4\ \mathrm{W} \\ P_{PM,loss} &= 314\ \mathrm{W} + 220\ \mathrm{W} = 534\ \mathrm{W} \end{aligned} \tag{4.5}$$

These losses are modelled as heat sources in the hydraulic system, while the electric motor losses are excluded from the thermal model (Section 5) since the PMSM is not in direct thermal contact with the hydraulic oil.

Overall, the results demonstrate that the EHA achieves more than three times the efficiency of the LS system under the Y-cycle, primarily due to reduced throttling losses and its capability for regenerative operation. In the present study, the LS system's variable displacement pump is operated at constant speed, which leads to increased losses under partial-load conditions, as the efficiency of the LS pump decreases at lower displacement settings. Since a PMSM is employed, a variable-speed LS implementation is technically feasible and could mitigate these losses, as demonstrated in [12]. Nevertheless, the constant-speed LS configuration represents the traditional load-sensing system architecture and is therefore an appropriate baseline for the present comparison.

The energy breakdown identifies the pump/motor unit as the dominant source of losses, while the auxiliary components contribute only marginally. These findings confirm the superior energy efficiency of the EHA, and the simulated power losses serve as an input in the subsequent thermal analysis.

5. THERMAL ANALYSIS

Thermal management is critical for EHAs, as their closed hydraulic circuit restricts heat dissipation. Unlike centralised hydraulic systems, where oil continuously returns to a reservoir providing effective cooling, the closed-circuit design of an EHA limits heat rejection and leads to higher temperatures. Elevated temperature lowers viscosity, weakens lubrication, and accelerates component wear. This analysis predicts system temperature over the continuous Y-cycle and evaluates the need for additional cooling.

A lumped-parameter model with a single combined control volume, representing the thermal capacities of the fluid and surrounding solids, is used. It defines a single system temperature T and an ambient temperature $T_{sur} = 20$ °C. The model combines convective cooling described by Newton's law of cooling and radiative heat exchange based on the Stefan–Boltzmann law. The oil is assumed to be well mixed, and all losses identified in Section 4.2 are represented as a constant cycle-averaged total heat input P_{loss}.

The system's thermal dynamics are

$$C\frac{dT}{dt} = P_{loss} - Q \qquad\qquad Q = \sum_i \frac{T - T_{sur}}{R_{th,i}} \tag{5.1}$$

The lumped heat capacity of the oil and the components is

$$C = c_{p,oil}m_{oil} + \sum_i c_{p,i}m_i \tag{5.2}$$

where c_p denotes specific heat capacity and m mass. Thermal resistances are

$$R_{th,i} = \frac{1}{\left(h_{conv,i} + h_{rad,i}\right)A_{s,i}} \tag{5.3}$$

where $A_{s,i}$ is the surface area of the component.

The radiative and convective heat transfer coefficients are expressed as

$$h_{rad} = \varepsilon\sigma(T^2 + T_{sur}^2)(T + T_{sur}) \qquad\qquad h_{conv} = \frac{Nu \cdot k}{l_c} \tag{5.4}$$

where ε is the surface emissivity, $\sigma = 5.67 \cdot 10^{-8}\ \mathrm{W/(m^2K^4)}$ is the Stefan-Boltzmann constant [25], k is the thermal conductivity of air evaluated at the reference temperature $\bar{T} = (T + T_{sur})/2$, and l_c is the characteristic length of the component. The Nusselt number is geometry-dependent, and simple geometries such as horizontal cylinders and cubes are therefore adopted. The correlations used to calculate the Nusselt numbers for air free convection for the considered geometries are given in Table 3. Heat transfer is assumed to be governed by free convection and radiation, while forced convection resistances associated with internal pipe flow are neglected.

The dimensionless parameters are

$$Nu = \frac{hl_c}{k} \qquad\qquad Pr = \frac{\rho\nu c_p}{k} \qquad\qquad Gr = \frac{gl_c^3\beta_{air}\Delta T}{\nu^2} \tag{5.5}$$

where Pr is the Prandtl number, Gr the Grashof number, ρ the density, ν the kinematic viscosity, $g = 9.81\ \mathrm{m/s^2}$, and β_{air} the thermal expansion coefficient of air.

The oil heat capacity is updated with temperature following [26]:

$$c_p(T) = c_0 + \alpha_c(T - 273.15) \qquad c_0 = 1807\ \frac{\mathrm{J}}{\mathrm{kg \cdot K}} \qquad \alpha_c = 4.21\ \frac{\mathrm{J}}{\mathrm{kg \cdot K^2}} \tag{5.6}$$

Air is modelled as an ideal gas for evaluating density and thermal expansion:

$$\rho_{air} = p/(R_{air}\bar{T}) \qquad \beta_{air} = 1/\bar{T} \tag{5.7}$$

All other air properties are interpolated from tabulated data from [27]. Thermophysical properties are updated continuously using these relations.

Table 3: Nusselt correlations for free convection geometries [27, 28]. Air properties evaluated at the reference temperature.

Geometry	Nusselt number
Horizontal cylinder	$Nu = \left[0.6 + 0.387(Gr\ Pr)^{1/6}\left(1 + (0.559/Pr)^{9/16}\right)^{-8/27}\right]^2$ $Gr = Gr(T - T_{sur}),\ l_c = d$
Cube	$Nu = 5.748 + 0.752(Pr\ Gr)^{0.252}\left[1 - (0.492/Pr)^{9/16}\right]^{-0.448}$ $Gr = Gr(T - T_{sur}),\ l_c = A/D,\ D = \sqrt{4A_{proj}/\pi}$

Figure 5.1 shows the simulated temperature rise under continuous load-cycle operation. The system temperature approaches 82 °C after 350 min. The hydraulic system temperature exceeds the typical operating range of hydraulic systems (50–60 °C) [29] after about 85 min, indicating that additional cooling is required for long-term reliability. Internal forced convection resistances are omitted, which overestimates heat rejection. The actual cooling capacity may therefore be lower in practice. Furthermore, component power losses depend on the temperature in the real system, so the heat generation in the model may be slightly underestimated.

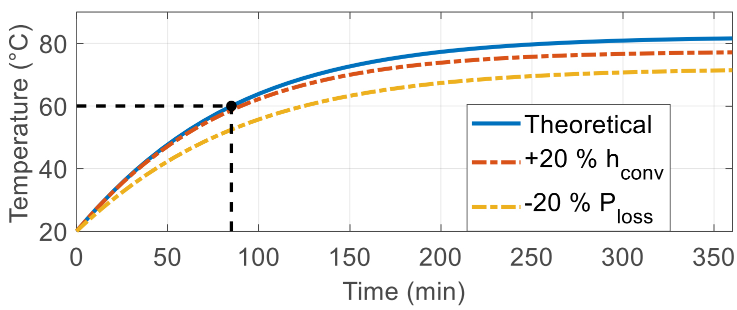

Figure 5.1. Simulated system temperature rise under continuous operation.

Jungnickel (2010, as cited in [14]) reported that natural convection coefficients may exceed theoretical estimates by up to 20 %. Moreover, Ketelsen et al. [14] showed that the results can be highly sensitive to power loss modelling errors. The present sensitivity analysis indicates that increasing the natural convection heat transfer coefficient by 20 % lowers the steady-state temperature by roughly 5 °C, whereas a 20 % reduction in input heat lowers it by about 10 °C. Even in the most favourable case, the temperature remains above the recommended range, indicating that active cooling is required for reliable long-term operation.

Thermal resistances of the components at the steady state temperature are listed in Table 4. These values are updated during the simulation, as they vary with temperature.

Table 4: Heat transfer coefficients and thermal resistances of system components at the steady-state temperature.

Component	Geometry	A_s [cm^2]	l_c [mm]	ε	h_{conv} [W/m^{2}K^{-1}]	h_{rad} [W/m^{2}K^{-1}]	R_{th} [K/W]
Pump	Cube	1350	798	0.90	12.7	7.00	0.376
Hoses	Cylinder	3970	16.2	0.93	8.59	7.24	0.159
Cylinder	Cylinder	4182	104	0.90	6.01	7.00	0.184
Accumulator	Cylinder	1297	200	0.90	5.59	7.00	0.612

6. CONCLUSION

This study evaluated the performance of electro-hydrostatic actuators for wheel loader work functions through simulations based on measured load cycle and external load data. The analysis covered controllability through position tracking precision, energy efficiency in comparison with an LS system, and thermal behaviour using a lumped-parameter model suitable for early-stage evaluation.

The main findings are:

- EHAs achieved satisfactory tracking accuracy, although the load-holding valve caused transient errors. The maximum tracking errors were below 4 mm for the lift actuator and 29 mm for the tilt actuator, with RMS errors of 1.3 mm and 5.4 mm, respectively.
- EHAs required only 31.9 % of the LS system's electrical input for the same work cycle, corresponding to efficiencies of 55.1 % and 17.0 % for the EHA and LS systems, respectively.
- Thermal simulations showed that the EHA exceeded typical hydraulic operating temperatures, indicating the need for additional cooling. The steady-state temperature reached 82 °C with theoretically calculated heat transfer coefficients, and ±20 % variations in these coefficients or heat inputs did not change this conclusion.

These results demonstrate that EHAs provide significant efficiency improvements compared with the LS system, but thermal management must be addressed to ensure reliable operation in such applications. In the present study, active cooling of the EHAs would have been required, which may compromise the efficiency benefits.

ACKNOWLEDGMENTS

This work was supported by Business Finland's Drive Forward project [ref. 428/31/2024].

REFERENCES

[1] Pustavrh, J., Hočevar, M., Podržaj, P., Trajkovski, A., Majdič, F., 'Comparison of hydraulic, pneumatic and electric linear actuation systems', Scientific Reports, 13(1), Article 20938, 2023, https://doi.org/10.1038/s41598-023-47602-x.

[2] Wiens, T., Deibert, B., 'A Low-Cost Miniature Electrohydrostatic Actuator System', Actuators, 9(4):130, 2020, https://doi.org/10.3390/act9040130.

[3] Padovani, D., Rundo, M., Altare, G., 'The Working Hydraulics of Valve-Controlled Mobile Machines: Classification and Review', Journal of Dynamic Systems, Measurement, and Control, 142(7), Article 070801, 2020, https://doi.org/10.1115/1.4046334.

[4] Niemelä, J., Vuorinen, E., Orifjonov, A., et al., Machinopedia—Review of Electric and Hybrid Off-Road Mobile Machines, Tampere University, 2024. Available: https://trepo.tuni.fi/bitstream/handle/10024/159633/978-952-03-2980-8.pdf. Accessed: Sep. 30, 2025.

[5] Minav, T., Bonato, C., Sainio, P., Pietola, M., 'Efficiency of direct driven hydraulic drive for non-road mobile working machines', 2014 International Conference on Electrical Machines (ICEM), Article 6960527, 2014, https://doi.org/10.1109/ICELMACH.2014.6960527.

[6] Agostini, T., De Negri, V., Minav, T., Pietola, M., 'Effect of Energy Recovery on Efficiency in Electro-Hydrostatic Closed System for Differential Actuator', Actuators, 9(1), Article 12, 2020, https://doi.org/10.3390/act9010012.

[7] Minav, T., Lehmuspelto, T., Sainio, P., Pietola, M., 'Series Hybrid Mining Loader with Zonal Hydraulics', IFK 2016, Dresden, Germany, 8-10 Mar. 2016.

[8] Zhang, S., Minav, T., Pietola, M., 'Decentralized Hydraulics for Micro Excavator', 15th Scandinavian International Conference on Fluid Power (SICFP'17), Linköping, 2017, pp. 187–195.

[9] Casoli, P., Scolari, F., Minav, T., Rundo, M., 'Comparative Energy Analysis of a Load Sensing System and a Zonal Hydraulics for a 9-Tonne Excavator', Actuators, 9(2), Article 39, 2020, https://doi.org/10.3390/act9020039.

[10] Pietrzyk, T., Roth, D., Schmitz, K., Jacobs, G., 'Design study of a high speed power unit for electro hydraulic actuators (EHA) in mobile applications', 11th International Fluid Power Conference, Aachen, Germany, 2018, pp. 233–245.

[11] Figge, F., Schmitz, K., 'Simulative Comparison Approach of Electro-Hydrostatic Actuator Circuits in Excavators', ASME/BATH 2023 Symposium on Fluid Power and Motion Control, Florida, Oct. 2023, https://doi.org/10.1115/FPMC2023-111798.

[12] Wang, F., Qiao, Y., Zhou, H., Wu, J., Xu, B., 'An Independent Electro-Hydraulic Variable Speed Drive to Improve Energy Efficiency of Electric Wheel Loader Working System', IEEE Transactions on Vehicular Technology, 73(12), 18250–18265, 2024, https://doi.org/10.1109/TVT.2024.3438268.

[13] Minav, T., Papini, L., Järf, A., Tammi, K., Pietola, M., ‘Direct Driven Hydraulics: What can possibly go wrong? –A thermal analysis’, 2016 XXII International Conference on Electrical Machines (ICEM), Lausanne, Switzerland, pp. 1618-1624, 2016, https://doi.org/10.1109/ICELMACH.2016.7732740.

[14] Ketelsen, S., Michel, S., Andersen, T., Ebbesen, M., Weber, J., Schmidt, L., ‘Thermo-Hydraulic Modelling and Experimental Validation of an Electro-Hydraulic Compact Drive’, Energies, 14(9), Article 2375, 2021, https://doi.org/10.3390/en14092375.

[15] Michel, S., Schulze, T., Weber, J., ‘Energy-efficiency and thermo energetic behaviour of electrohydraulic compact drives’, 9th International Fluid Power Conference, Aachen, Germany, 24–26 March 2014.

[16] Michel, S., Weber, J., ‘Prediction of the thermo-energetic behaviour of an electrohydraulic compact drive’, 10th International Fluid Power Conference, Dresden, Germany, 8–10 March 2016, pp. 219–234.

[17] Linjama, M., Huova, M., Tammisto, J., Tervonen, J., Ahola, V., ‘6-ton wheel loader short Y-cycle data for 440 seconds loading of gravel’, Zenodo, 2024, https://doi.org/10.5281/zenodo.10639199.

[18] Bosch Rexroth AG, MS2N Synchronous Servomotors: Project Planning Manual, Document R911347583, Edition 07, 06/2021.

[19] Huova, M., Tammisto, J., Linjama, M., Tervonen, J., ‘Fuel Efficiency Analysis of Selected Hydraulic Hybrids in a Wheel Loader Application’, BATH/ASME 2018 Symposium on Fluid Power and Motion Control, Bath, UK, Sept. 12–14, 2018, V001T01A035, https://doi.org/10.1115/FPMC2018-8869.

[20] Vasiliu, N., Vasiliu, D., Călinoiu, C., Puhalschi, R., Simulation of Fluid Power Systems with Simcenter Amesim, 1st ed., CRC Press, 2018, ISBN 978-1482253559.

[21] ENGIRO GmbH, Data sheet 260W-08058-ABC, ver. 14.01, July 2025. Available: https://www.engiro.com/fileadmin/pdfs/Datenblaetter_engiro/260W/ENGIRO_Datasheet_260W_08058_ABC_V14_01.pdf. Accessed: Aug. 25, 2025.

[22] Kim, S.-H., Electric motor control: DC, AC, and BLDC motors, Elsevier, 2017.

[23] Jensen, K.J., Ebbesen, M.K., Hansen, M.R., ‘Novel Concept for Electro-Hydrostatic Actuators for Motion Control of Hydraulic Manipulators’, Energies, 14(20), 6566, 2021, https://doi.org/10.3390/en14206566.

[24] Schmidt, L., Ketelsen, S., Mommers, R., Achten, P., ‘Analogy between hydraulic transformers & variable-speed pumps’, BATH/ASME 2020 Symposium on Fluid Power and Motion Control, 2020, Article V001T01A007, https://doi.org/10.1115/FPMC2020-2719.

[25] Çengel, Y., Cimbala, J., Turner, R., Fundamentals of Thermal-Fluid Sciences, 5th ed., McGraw-Hill Education, 2016, ISBN 978-0078027680.

[26] Busquets, E., Ivantysynova, M., ‘Temperature Prediction of Displacement Controlled Multi-Actuator Machines’, International Journal of Fluid Power, 14(1), 25-36, 2013, https://doi.org/10.1080/14399776.2013.10781066.

[27] VDI-GVC, VDI Heat Atlas, 2nd ed., Springer, Berlin, 2010, https://doi.org/10.1007/978-3-540-77877-6.

[28] VDI-GVC, VDI-Wärmeatlas, 11th ed., Springer, Berlin, 2013, https://doi.org/10.1007/978-3-642-19981-3.

[29] Ponomarev, P., Åman, R., Handroos, H., Immonen, P., Pyrhönen, J., Laurila, L., ’High power density integrated electro-hydraulic energy converter for heavy hybrid off-highway working vehicles’, IET Electrical Systems in Transportation, 4(4), 114–121, 2014, https://doi.org/10.1049/iet-est.2013.0009.

Biographies

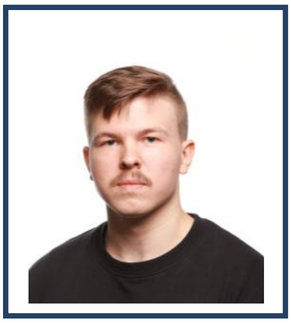

Vili Vironmäki received the bachelor's degree in automation engineering from Tampere University in 2025. He is currently pursuing the master's degree in automation engineering at Tampere University, where he also works as a Research Assistant in the Automation Technology and Mechanical Engineering Unit, Faculty of Engineering and Natural Sciences. His research interests include electro-hydrostatic actuator modelling and control.

Ville Raunio received the bachelor's degree in automation engineering from Tampere University in 2023. He is currently pursuing the master's degree in automation engineering at Tampere University. He is currently working as a Model-Based Design Trainee at Epec Oy. His areas of interest include model-based design and electrification of mobile machinery.

Mikko Huova received the M.Sc. in automation engineering in 2008 and completed his Ph.D. in the same field in 2015, both from Tampere University of Technology. He is currently working as a Senior Research Fellow at the Automation Technology and Mechanical Engineering unit at Tampere University. The areas of interest include energy efficient actuator systems, mobile machinery and model-based control.

Petteri Multanen received the master's degree in mechanical engineering from Tampere University of Technology in 1996, and the philosophy of doctorate degree in Electrical-Electronics & Computer Engineering from Tampere University of Technology in 2002. He is currently working as a University Lecturer at the Automation Technology and Mechanical Engineering Unit, Faculty of Engineering and Natural Sciences in Tampere University. His research areas include hybrid drives and energy efficient mobile machines.